WELDING RESEARCH

SUPPLEMENT TO THE *WELDING JOURNAL,* FEBRUARY 2015
Sponsored by the American Welding Society and the Welding Research Council

Interfacial Temperature Profiles in Simulated Resistance Spot Welding of Bare and Zinc-Coated Steel

Temperature profiles were measured using infrared emission monitoring and analyzed for better understanding of basic phenomena in RSW

BY E. KIM AND T. W. EAGAR

ABSTRACT

For better understanding of basic phenomena of resistance spot welding, temperature profiles were measured by monitoring the infrared emissions at 5 kHz from one dimensionally simulated welding of sheet metal disks between the electrodes of a resistance spot welding machine. The weld variables included the zinc coating thickness, coating morphology, workpiece thickness, and electrode force.

For a given tap and heat control setting in the welding machine, as the coating thickness increased, the induced welding current increased due to a lower contact resistance created by the molten zinc layer. However, the temperatures experienced by the workpiece and electrode decreased. This was due to a decreased power absorption of the materials with lower electrical resistance of thicker coatings and the electrical characteristics of the spot welding machine. The temperature differences in welding of materials with different coating morphologies and specimen thicknesses are most pronounced at the faying interface. As the electrode force increased, the temperature differences between the materials decreased due to the decreased effect of the contact characteristics. The thicker material of bare steel became less sensitive to the contact characteristics as the electrode force increased. This was due to the decreased ratio of contact resistance to the total resistance. Thinner materials experience faster temperature rise and lose more heat to the electrodes.

KEYWORDS

• Temperature Profiles • Resistance Welding • Zinc Coated • Spot Weld

Introduction

To achieve a better understanding of the basic phenomena of resistance spot welding, it is very important to understand the transient behavior of temperature profiles. However, little work has been done due to the difficulties caused by the nature of the process. The time scale is a fraction of a second and the current is high enough to make the conventional electrical method using thermocouples infeasible. The infrared emission monitoring method presented in a prior paper by Kim and Eagar may be a good alternative even though it measures only the surface temperature (Ref. 1). Even though various numerical analyses and experimental work were performed in resistance spot welding, there are few studies to quantify the temperature profiles experimentally (Refs. 2–14).

In this research, the temperature profiles were measured using the infrared emission monitoring method during simulated disk welding. To eliminate the effects of the electrode and workpiece geometry, the experiment was performed using the modified welding setup as depicted in Fig. 1. As was described in Ref. 1, the surface of the cylindrical section of the electrodes and disk coupons were painted with temperature-sensitive lacquer, which remains solid to 1371°C. The emissivity of this lacquer was calibrated by comparing the infrared temperature measurement with thermocouple readings on a statically heated sheet held at various temperatures.

Even though the measured temperature profiles do not represent a full sheet weld, this method is believed to be very informative to see the relative effects of welding variables including the zinc coating thickness, coating morphology, electrode force, and the workpiece thickness. These results will help understand the basic phenomena of resistance spot welding, particularly the characteristics of the electrode/workpiece interface and the faying interface, which are inaccessible by other methods.

Experimental Procedures

Figure 1 shows the experimental equipment setup and a typical temperature profile developed in the disk

E. KIM (keuiwhan@ajou.ac.kr) *is professor, Department of Systems Engineering, Ajou University, Suwon, Republic of Korea. T. W. EAGAR* (tweagar@mit.edu) *is professor of Materials Engineering and Engineering Systems, Massachusetts Institute of Technology, Cambridge, Mass.*

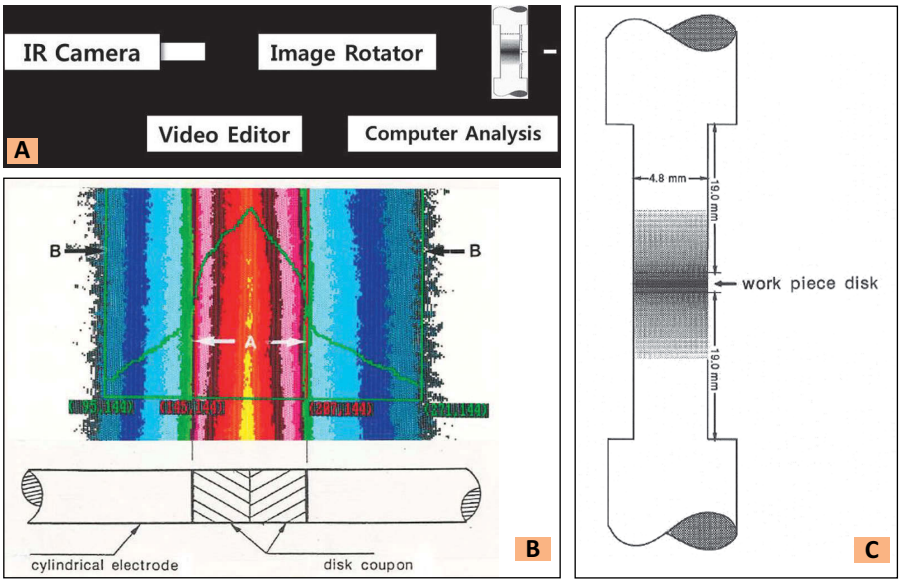

Fig. 1 — A — Experimental equipment setup showing infrared temperature-monitoring system. B — A typical temperature profile of a high-speed line scan along the axis of one dimensionally simulated disk welding; C — electrodes-workpiece setup (Ref. 1).

simulation experiment as has been reported previously (Ref. 1). In Fig. 1B, the two vertical lines marked A near the center show the location of the electrode interfaces. Another set of vertical lines marked B is 1.6 kN mm from the interface where the electrode temperature was measured. The temperature was also measured at the faying interface and the electrode interface. The temperature profile at the electrode interface was measured both at the electrode side and workpiece side. The measurement was performed when the highest temperature was reached at the faying interface. As would be expected, the temperature always reached its maximum value at the end of the weld cycle.

The variables studied in this experiment included changes in the electrode force as well as the zinc coating of the steel and the workpiece thickness. To see the effect of coating morphology, 0.8-mm hot dip galvanized steel (G60), galvannealed steel (A40), and electrogalvanized steel (E70) were used. Electrode forces of 1.6 kN (350 lb), 2.2 kN (500 lb), 2.9 kN (650 lb), and 3.5 kN (800 lb) were employed for this experiment. The effect of the coating thickness was tested using 0.8-mm electrogalvanized steels with four different coating thicknesses, i.e, 100 g/m^2 (AM100), 68 g/m^2 (AM68), 35 g/m^2 (AM35), and 0 g/m^2 (AMBR) of zinc on both sides. The bare steel was produced by etching away the zinc coating in a solution of HCl. The electrode force for this test was 2.2 kN. For the evaluation of workpiece thickness, 1.6-mm steel sheet was machined to 1.4 mm (BR14), 1.16 mm (BR12), 0.8 mm (BR08), 0.6 mm (BR06), and 0.5 mm (BR05). Using these specimens, welding was performed for each thickness. The electrode forces for these experiments were 1.8 kN (400 lb), 2.9 kN (650 lb), and 4.0 kN (900 lb). Welding of different thicknesses was also performed on combinations of 1.16- and 0.5-mm-thick materials using 2.9 kN as the electrode force.

Since this experiment used simulated disk welding, the welding current was reduced by inserting an electrically resistive material, such as Inconel® or stainless foil, between the electrode holder shank and the welding machine. By doing so, the temperature was kept low enough so that melting and collapse of the disk coupon would be avoided. During these experiments, the tap setting and the weld schedule were kept fixed to see the differences in the induced current for different surface conditions, workpiece thicknesses, and electrode forces.

In most cases, the data presented in this paper are the averages of the maximum temperatures observed for more than three measurements except for the experiments with varying material thickness in which uncoated steel sheets were used. For the material thickness, experiments, one measurement was made due to difficulties in preparing the weld specimens. The thinner experimental sheets were made by machining the thick material to the desired dimension. This was acceptable because bare steel welding is much more consistent than coated steel welding. There were some difficulties in the experiment with coated steel. The main difficulty was caused by variations in the electrode/workpiece contact. The electrode surface was pretreated by running 50 conditioning welds. After electrode conditioning, the electrode surface usually showed an even deposit of zinc on the face.

In real welding, even a very small misalignment of the electrodes and specimen is great enough to cause uneven heating of the disk coupons. Thus, if the temperature profile did not show acceptable symmetry in the upper and lower electrodes, it was judged that uneven heating had occurred and the data were discarded. Another difficulty in this experiment was the effect of the molten zinc. The liquid zinc was squeezed out to the edge of the interface and changed the emissivity of the surface. This was easily observed in the recorded data. For such cases, a large apparent temperature change could be seen near the interface. One other difficulty found during this experiment was peeling of the high-temperature paint, which was applied on the side surfaces of electrodes and workpieces to keep the infrared emissivity constant (Ref. 1). The peeling was usually accompanied by a large vertical displacement of the electrodes (or collapse of the disk coupon). These data were also excluded.

Results and Discussion

Effect of Coating Thickness

Table 1 shows the temperature data measured at the end of current flow. The induced currents are also listed in this table. The effect of coating thickness is clearly seen in this table. These data are plotted in Fig. 2A and B for comparison.

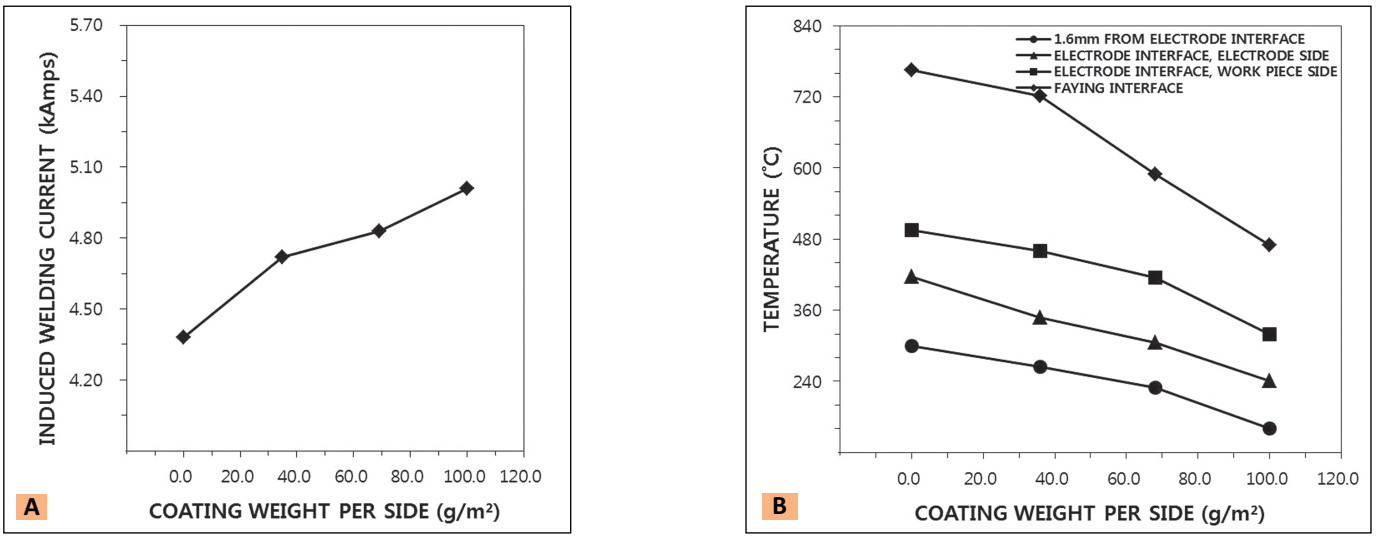

Fig. 2 — Effect of coating thickness on A — the induced welding current; B — temperature; in simulated disk welding.

As the coating thickness increases, the induced current increases. For bulk material, it is obvious that an increase in thickness should increase electrical resistance and thus decrease the induced current. However, in resistance spot welding, the total electrical resistance is comprised of bulk resistance and contact resistance. The electrical resistance of the zinc coating behaves as a contact resistance rather than a bulk resistance. In this experiment, the thickness of the coating ranges from 0 to 14 μm, which is negligible compared to the thickness of the workpiece of 0.8 mm. As the coating thickness and temperature during welding increase, the interface contacts more closely resulting in reduced contact resistance. This leads to the decrease in total resistance and thus the increase in the induced current for a given welding machine setting.

However, as the coating thickness increases, the temperatures are lower due to the decreased total power input to the workpiece. This can be explained by considering the electrical characteristics of the resistance spot welding machine (Refs. 16, 17). That is, the induced weld current decreases as the resistance of the workpiece increases. Nonetheless, the induced voltage increases with increasing workpiece resistance. As the absorbed power is a product of current and voltage, this absorbed power increases with increasing resistance and then decreases, showing a maximum value at a certain resistance value. Spot welding is usually performed below this resistance value. Thus, decreasing the resistance of the workpiece will decrease the power delivered to the weld even though the induced current increases.

Table 1 — Effect of Coating Thickness on Temperature

Material	Faying Interface	Electrode Interface (workpiece side)	Electrode Interface (electrode side)	Electrode (1.6 mm from electrode interface)	Induced Current (kA)
AM100	467	313	233	165	5.01
AM68	589	415	298	229	4.83
AM35	722	460	347	260	4.72
AMBR	766	491	419	297	4.37

Temperature in °C, 2.2 kN (500 lb) electrode force.

This shows the importance of electrical contact resistance along with the thermal contact conductance in the nugget growth mechanism. It is easy to conceive that materials with harder contact surfaces have higher electrical contact resistance and thus a lower interfacial heat transfer coefficient. This is based on the explanation of Holm and Kim that (electrical contact resistivity) × (interfacial heat transfer coefficient) is a function of temperature and has a reciprocal relationship (Refs. 18, 19). Thus, materials with thicker coatings show lower electrical contact resistance and higher interfacial heat transfer coefficient. The electrode temperature was observed to be higher with decreasing coating thickness. In Table 1, it is seen that the hardest contact surface material, in this case the bare steel, showed the highest temperature in the electrodes. If the electrical contact resistance and the thermal contact resistance are considered together, it is not clear which one contributes more to the electrode temperature.

The temperature data discussed thus far can be related to the welding behavior of these materials. Figure 3 shows the welding current requirement vs. coating weight for the same materials used in this experiment (Ref. 15). Horita et al. also reported that the increase in zinc coating thickness resulted in a higher current requirement for the same nugget size (Ref. 2). Figure 3 can be explained qualitatively using the current and temperature data. As the coating weight increases, the required current increases due to the lower heat generation rate coupled with a higher heat dissipation rate into the electrodes. The demand of higher welding current with thicker coating material is due to the decreased electrical contact resistance and lower power absorption along with the increased heat dissipa-

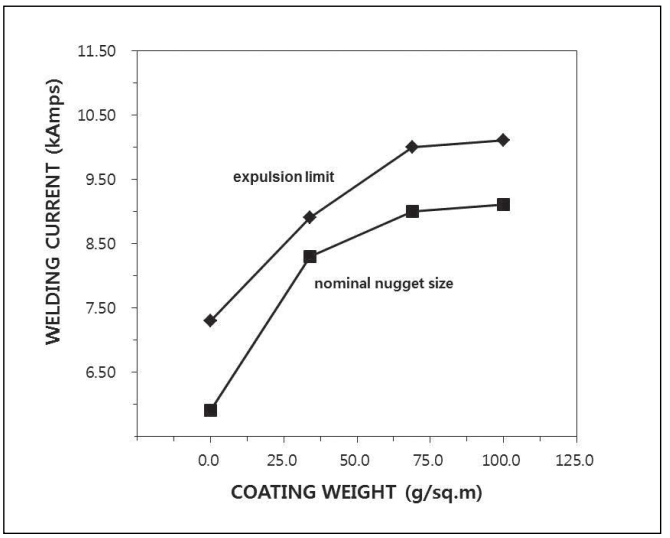

Fig. 3 — Effect of coating weight on current requirement (Ref. 2).

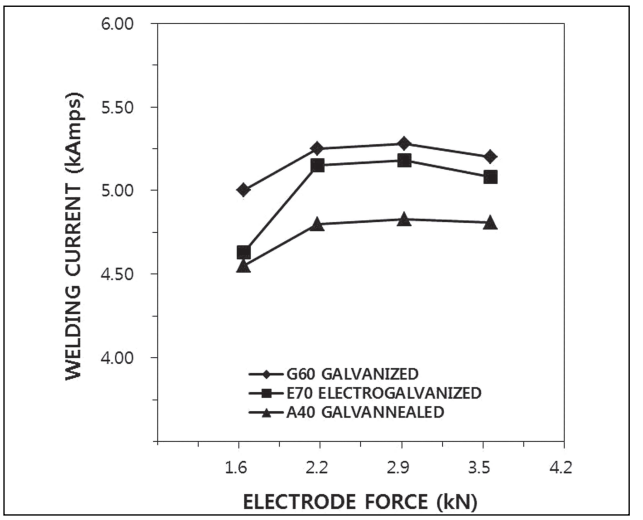

Fig. 4 — Effect of zinc-coating morphology and electrode force on the induced welding current in simulated disk welding.

tion at the electrode interface as discussed previously in this section. The heat generation rate at the faying interface also decreases with the formation of a larger halo with thicker zinc coatings. The larger halo increases the current flow area and thus decreases the current density at the faying interface. This illustrates the importance of the thermal contact resistance at the electrode interface in the nugget growth mechanism. This observation may explain the reason why spot welding of galvanized sheets requires a higher current level compared to bare materials. Previously, the formation of a zinc halo surrounding the weld nugget was the common explanation for the effectively larger nugget size and consequently the higher current requirement when welding galvanized materials (Refs. 2–4). In addition to this halo effect, the enhanced heat transfer characteristics at the electrode interface of the zinc-coated steel is also seen to be important. As the nugget size increases, the heat loss to the electrode becomes greater and will demand higher heat input.

Effect of Coating Morphology under Various Electrode Forces

The effect of coating morphology and the sensitivity of the coated sheet materials to the electrode force was also investigated. Figure 4 shows the induced welding current for three different coating morphologies, G60, E70, and A40. Figure 5A, B, and C shows the temperature changes at the faying interface, at the electrode interface on the coupon side, on the electrode interface at the electrode side, and in the electrodes 1.6 mm from the electrode contact interface with varying electrode forces. The temperature differences between materials are plotted again in Fig. 6A–D. The missing data points are due either to satura-

Table 2 — Effect of Coating Morphology on Temperature

Material	Faying Interface	Electrode Interface (workpiece side)	Electrode Interface (electrode side)	Electrode (1.6 mm from electrode interface)	Induced Current (kA)
A40	673	498	380	252	4.83
G60	604	479	367	242	5.3
E70	581	481	357	231	5.19

Temperature in °C, 2.9 kN (650 lb) electrode force.

Table 3 — Temperature Changes During Welding Dissimilar Thickness

Weld Cycle	Electrode 1.16 mm from Interface	1.16 mm Electrode Interface (electrode side)	Electrode Interface (workpiece side)	Maximum Temperature in the Specimen	Electrode Interface (workpiece side)	0.5 mm Electrode Interface (electrode side)	Electrode 1.16 mm from Interface
1	–	–	200	271	222	–	–
2	–	–	222	300	234	175	–
3	–	248	362	462	366	237	–
4	–	252	396	476	381	260	175
5	–	323	503	619	481	327	258
6	202	337	503	627	467	330	258
7.5	237	337	490	627	477	342	286
9.5	244	318	469	537	420	332	279
11	241	290	400	458	381	318	271
12	233	304	381	440	362	311	264

Temperatures in °C, 2.9 kN (650 lb) electrode force.

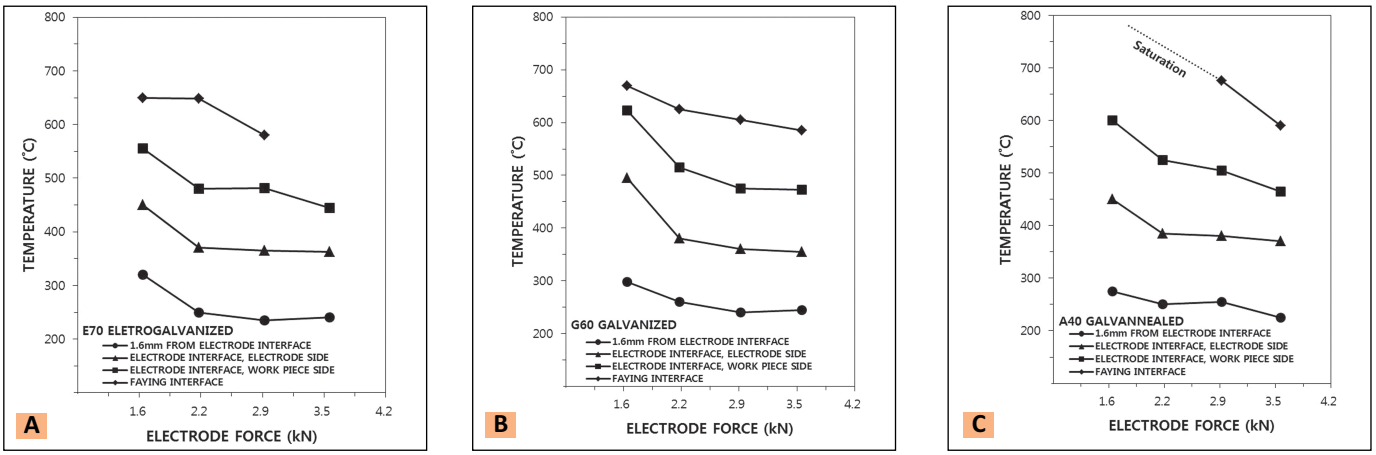

Fig. 5 — Temperature profiles in simulated disk welding for different coating morphologies. A — E70; B — G60; C — A40.

tion of the detector or to measurement of too large a value to be plotted on the same graph.

As could be expected from the above section, the hard surface galvanealed material, A40, shows lower induced current with relatively higher temperatures. The most conspicuous temperature difference can be found at the faying interface. The temperatures in the electrodes and at the electrode interfaces do not show any significant differences especially at high electrode forces. It seems that the differences are a little greater with the lowest electrode force. However, the temperature difference at the faying interface is much more pronounced during low electrode force welding. This may imply that the effect of coating morphology on weld temperature is more likely to be significant at the faying interface than at the electrode interface. The surface of A40 is composed of Fe-Zn compounds. These compounds are generally very hard and have a high melting temperature. The contact between Fe-Zn compounds and electrodes can resist severe deformation and can maintain higher electrical contact resistance even at elevated temperatures in comparison to the contact between copper electrodes and free zinc. For example, the dissociation temperature of one of the Fe, Zn, Γ compounds is about 780°C (Ref. 20). A40 galvannealed steel generally shows the thermal characteristics of a bare steel. This material has a hard interface similar to bare steels. In contrast, the materials with free zinc surfaces, E70 and G60 in this case, have softer interfaces. However, if the

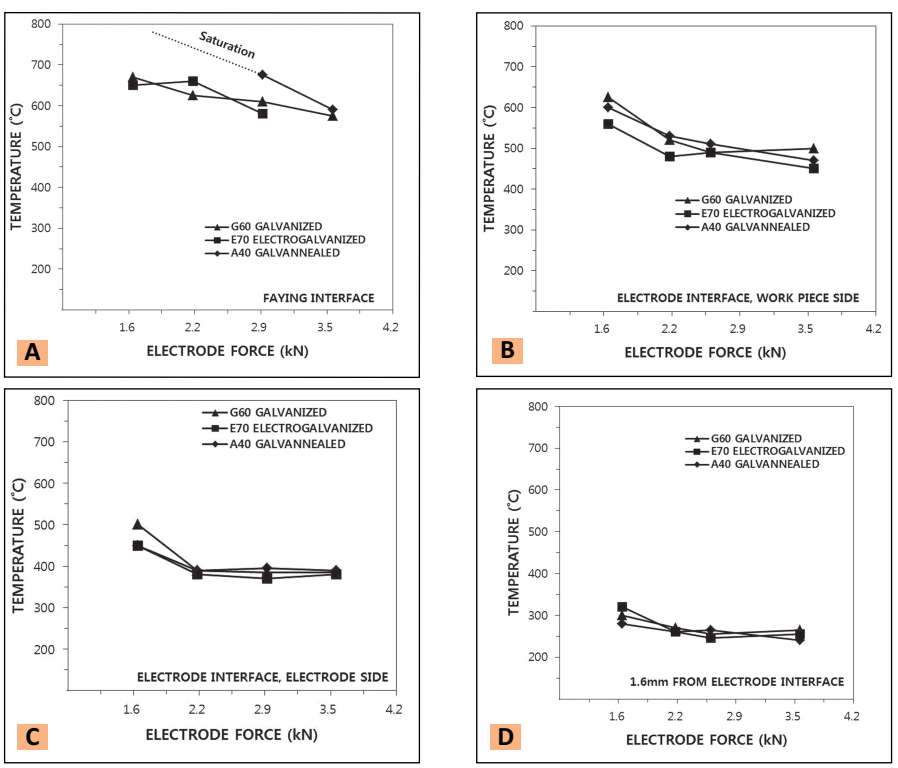

Fig. 6 — Temperature changes with varying electrode forces and coating morphologies at A — faying interface. B — Electrode interface at workpiece side; C — electrode interface at electrode side; D — electrode temperature at 1.6 mm from the electrode interface; in simulated disk welding.

electrode force is high enough, the effect of differences in surface morphology seems to become less, particularly at the electrode interface. The pressure of the electrode contact is about 400 MPa, which is more than half of the yield strength of the Cu-Cr electrode alloy. The high electrode force is coupled with high temperatures during welding. As a consequence, the interface deforms very easily, making differences in the heat transfer coefficient and the electrical resistivity very small in the early stages of welding. It seems that the faying interface temperature is less sensitive to the electrode force than is the temperature at other locations. At the lowest electrode force employed in this experiment, i.e., 1.6 kN, the highest interface temperatures and electrode temperatures were observed. At more

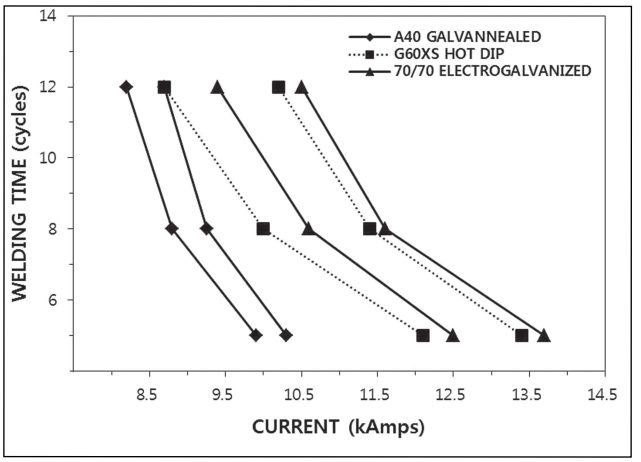

Fig. 7 — Lobe curves of zinc-coated materials (Ref. 1).

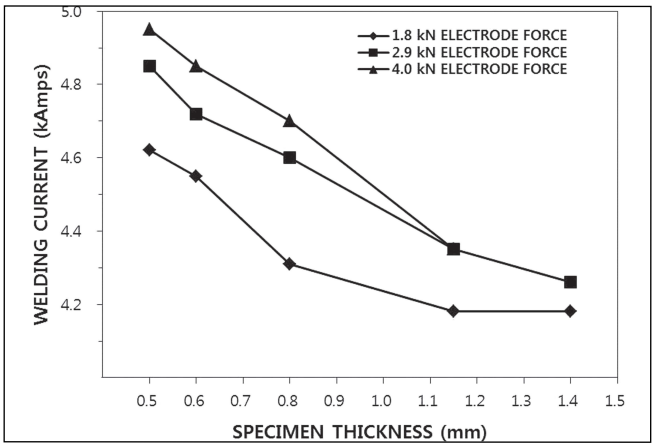

Fig. 8 — Effects of specimen thickness and electrode force on the induced current in simulated disk welding of bare steel.

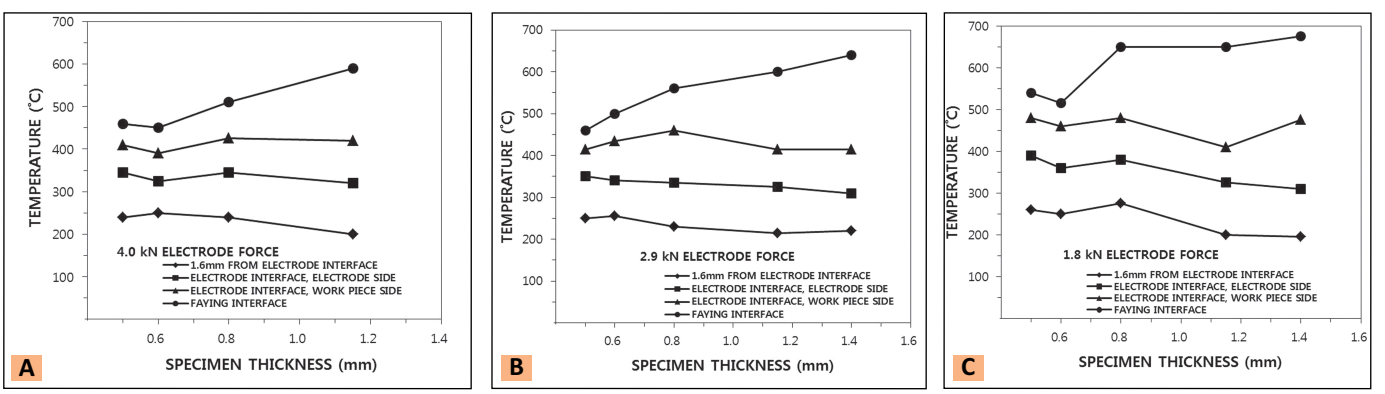

Fig. 9 — Temperature profiles in simulated disk welding of specimens of different thicknesses using A — 4.0 kN; B — 2.9 kN; C — 1.8kN of electrode force.

than 2.2 kN, the electrode force appeared to have an effect only at the faying interface. This can be explained by the same argument discussed in the previous section, i.e., greater deformation of the electrode surface and the coated workpiece surface occurs at elevated temperatures with high electrode forces. The temperature data for 2.9 kN electrode force are given in Table 2. The temperature differences at the electrode interface are much smaller than those at the faying interface. This supports the conclusion that the condition of the faying interface is more important than the electrode interface in terms of the nugget temperature development when using high electrode forces.

Generally speaking, the temperature decreases as the electrode force increases. However, the induced welding current increases with electrode forces, as shown in Fig. 5. This may be explained by the decreasing electrical and thermal contact resistances produced with the increasing electrode force. This explanation matches with the experimental measurement of contact resistance (Refs. 21–23). The effect of coating morphology on temperature development is also a function of the electrode force — Fig. 6. The effect is more pronounced at the faying interface when using high electrode forces. The final lobe shape will depend on the combined effect of these two contact resistances. Figure 7 shows the lobe curves for these coated materials (Ref. 1). The relative positions of the lobe curve qualitatively matches the thermal behavior observed in this experiment.

Effect of Welding Materials of Varying Thickness

Figure 8 shows the induced current for various electrode forces and specimen thicknesses. These were measured during the simulated welding of uncoated steel disk coupons. As expected, the induced current decreased as the specimen thickness increased. It is obvious that the thicker specimen has higher total electrical resistance. The effects of electrode force on the induced current for different specimen thicknesses are also seen in Fig. 8. It is clear that the effect of electrode force decreases as the specimen thickness increases. This can be explained by the decreased portion of electrical contact resistance in comparison with the total resistance during welding of thicker material. As the bulk resistance comprises a greater portion of the total resistance, the relative contribution of the contact resistance to the total resistance becomes less significant. As is shown in Fig. 8, the effect of changes in electrode force on the induced current is much greater when welding thinner material. This is believed to support the explanation given above.

As was introduced in the previous paragraph, the difference in current decreases as the electrode force increases. This is particularly pronounced in thick materials as

explained previously. In thinner materials where the contribution of contact resistance to the total resistance is believed to be more significant, the difference in the induced current between a 4.0 kN weld and a 2.9 kN weld is much smaller than that between 2.9 and 1.8 kN. This is believed to be related to the decreasing effect of the electrode force on the electrical contact resistance. As the electrode force increases, the relative change in the contact resistance will decrease.

Figure 9A–C shows the temperature data measured during simulated disk welding of bare steel with various electrode forces and specimen thicknesses. These temperature data are plotted again in Fig. 10A–D at each temperature measuring location. The three lines in each graph correspond to three different electrode forces.

In general, higher temperatures were observed during welding with lower electrode forces. The combined effects of larger electrical contact resistance, low thermal contact coefficient, and increased power input can explain these phenomena. However, as the specimen thickness increases, the effect of electrode force seems to decrease, as can be seen in Fig. 10. Again, this is explained by the relatively reduced contribution of electrical contact resistance to the total resistance. As the ratio of bulk resistance to the total resistance increases in the thicker materials, the sensitivity of the temperature profile to the electrode force decreases. This confirms that the ratio of electrical contact resistance to the bulk resistance can be a very important parameter in characterizing the nugget development mechanism as was discussed by Kim and Eagar previously (Ref. 24).

Figure 9 shows that the temperature difference between the faying interface and the electrode interface becomes larger as the specimen thickness increases. The temperature at the electrode interface and in the electrodes does not change much with increasing thickness, as can be seen in Fig. 10B–D. Only a very small decrease of the electrode interface temperature is present. However, the temperature increase at the faying interface is quite noticeable as in Fig. 10A.

The reason is most likely due to the shorter heat diffusion length within the workpiece. If the material is thin,

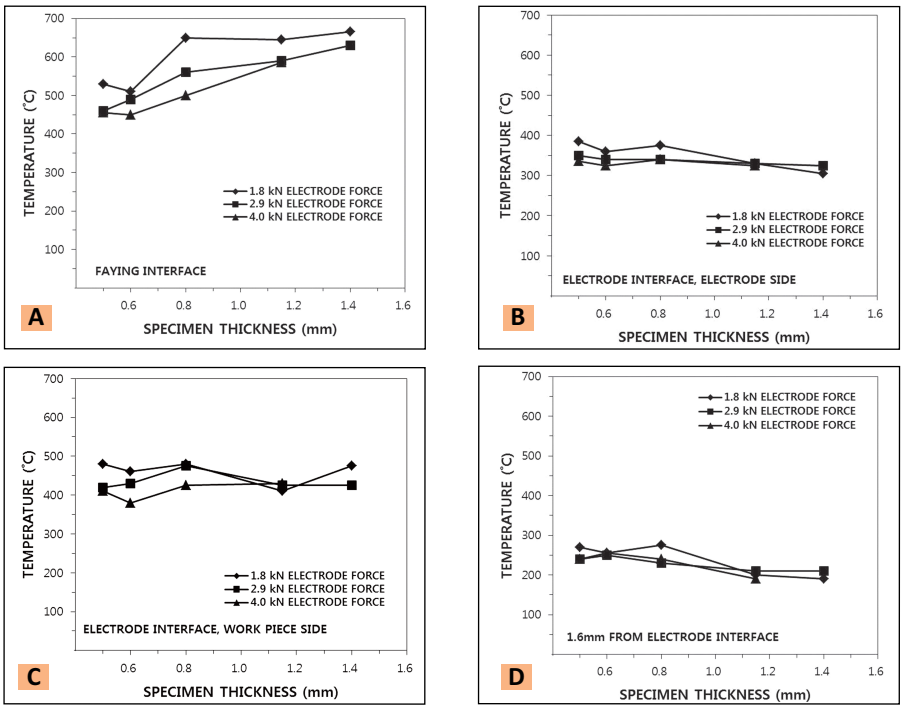

Fig. 10 — Temperature changes with varying electrode forces and specimen thickness at A — faying interface; B — electrode interface at electrode side; C — electrode interface at workpiece side; D — at 1.6 mm from the electrode interface in simulated disk welding.

the distance from the faying interface to the electrode interface is small. Therefore, the temperature profile across the specimen thickness shows a small temperature gradient. Higher temperatures at the electrode interface and in the electrodes for the thinner materials can be seen in Fig. 10B and D. However, the overall temperature is lower when welding thinner material. This seems to be related to the lower power input to the weld due to the smaller total resistance. When welding thick materials, the heat loss from the faying interface into the electrodes is less significant due to the greater heat diffusion length. The higher faying interface temperature is also related to the increased power. Thus, the higher faying interface temperatures with the thicker materials are possible due to the increased power absorption and the lower rate of heat loss into the electrodes.

Effect of Welding Materials of Different Thicknesses

To investigate the effect of specimen thickness, simulated disk welding on a combination of two different specimen thicknesses (1.16- and 0.5-mm-thick bare steels) was performed. A weld was made using 2.9 kN electrode force and exactly the same tap setting and welding schedule as was used during the other welding simulation. Thus, a comparison of the welding behavior of different thicknesses with the same current is possible.

The temperature changes during the course of welding are plotted in a cascade pattern in Fig. 11. The evolution and decay of temperature in both the thin and the thick materials clearly shows varying behavior. The temperature data from this figure are listed in Table 3. Figure 12 shows plots made with the data in Table 3. In these graphs, the temperature changes during welding are compared at various locations.

The temperature profiles at (a) and (b) in Fig. 11 show a faster temperature rise in the thin specimen. As the distance from the faying interface to the electrode interface is shorter on the thin material side, it is apparent that the thinner material is influenced more by heat generation from the faying interface. Thus in the early stages of welding, the workpiece temperature at the electrode interface is higher as compared with the thick side. In the

later stages of welding as in (c) and (d) in Fig. 11, the workpiece temperature at the electrode interface on the thick side increases more rapidly and surpasses the temperatures in the thin specimen. This is shown in Fig. 12. The thicker side also has a larger temperature discontinuity at the electrode interface. The breakdown of the electrode interface seems to occur much earlier on the thinner side due to the early buildup of heat in this part of the specimen. This means that more heat is lost to the electrode from the thinner side workpiece resulting in higher electrode temperature. A similar phenomenon was also observed in the case of spot welding of aluminum alloys, which has a lower melting point than steel (Ref. 25). As can be seen in (e) of Fig. 11, and thereafter, the electrode temperature is much higher in the thinner side electrode. This is clearly seen in Fig. 12D. Figure 12C also shows the slightly higher interface temperature of the electrode adjacent to the thin material.

The maximum temperature is found at the faying interface as a sharp peak. The peak at the faying interface is caused by heat generated due to the contact resistance. The temperature profile at (f) of Fig. 11 shows that the highest temperature in the workpiece is observed at the original faying interface location. However, as time elapses, the location of the highest temperature moves to the thicker specimen side. This is seen in (g) of Fig. 11 to the end. In these latter stages, the contact resistance of the faying interface does not appear to contribute to heat generation any longer. The evolution of temperature in the faying interface is plotted in Fig. 12D. The rapid rise of the temperature in the early stages of welding is known to be caused by the contact resistance. In the following stages of welding, the temperature rise is mostly due to heat generated in the body of the workpiece. Then the maximum temperature stays constant as one approaches the end of current flow. It seems that a steady state heat flux balance is established in the axial direction at this stage. The movement of the maximum temperature location is also believed to be related to a more symmetric heat loss to the electrodes.

At the end of weld current flow, the temperature profile in the workpiece becomes more symmetric as can be seen in (h) to (l) in Fig. 11. The temperature difference at the electrode interface also decreases as the temperature in the workpiece decreases. The electrode temperature on the thinner workpiece side experiences faster temperature rise and thus shows a higher electrode temperature and also a greater distance of heat propagation.

In this experiment, the major observation is that thin material experiences a faster temperature rise and loses more heat to the electrode resulting in higher electrode temperatures. The implication is that heat transferred across the electrode interface during welding of thin materials can be a much more important parameter than in the welding of thick materials.

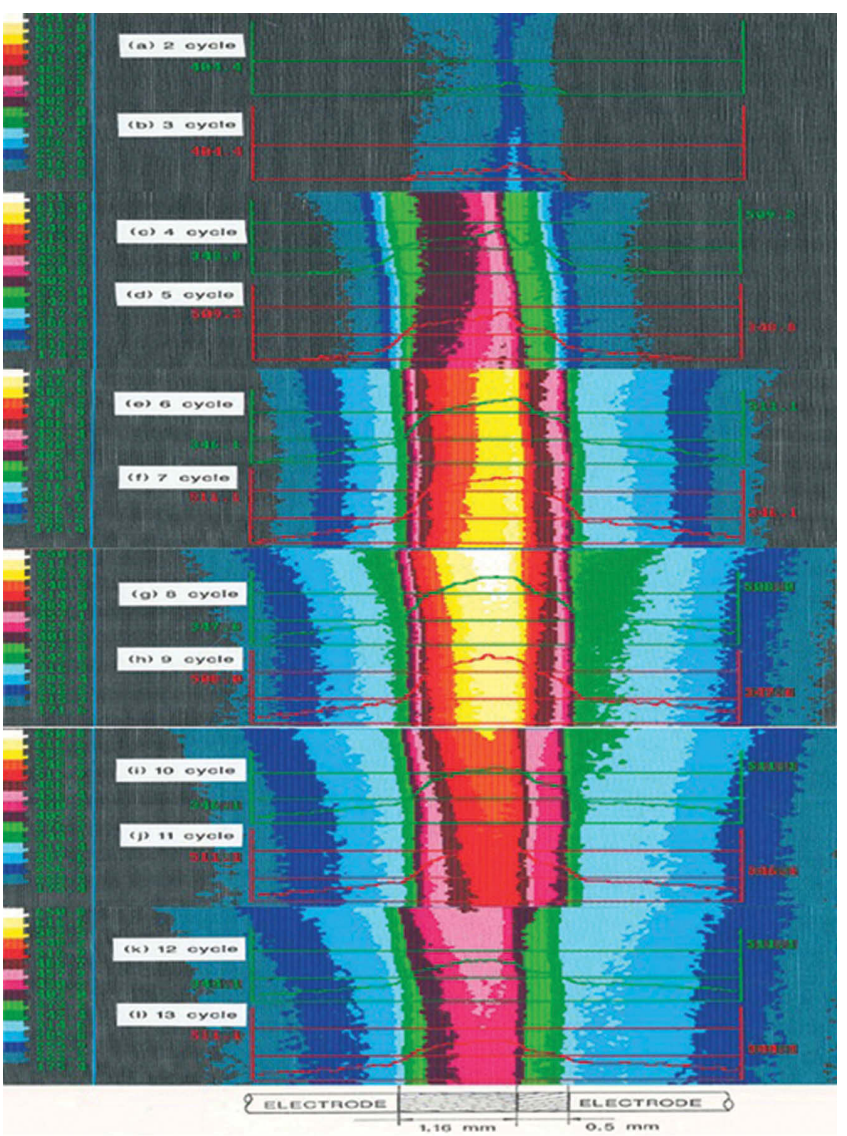

Fig. 11 — Cascade plot of temperature changes during simulated disk welding of bare steel of different thicknesses.

Conclusions

1) For a given tap and heat control setting on the welding machine, as the coating thickness increases, the induced welding current increases due to a lower contact resistance caused by the melted zinc and its halo. However, the temperatures experienced by the workpiece and the electrode decrease. This is due to a decreased power absorption of the materials with lower electrical resistance of thicker coatings and the electrical characteristics of the

spot welding machine.

2) The temperature differences in welding of materials with different coating morphology and specimen thickness are most pronounced at the faying interface.

3) As the electrode force increases, the temperature differences between materials decrease due to the decreased effect of the contact characteristics.

4) The thicker materials of bare steel become less sensitive to the contact characteristics as the electrode force increases. This is due to the decreased ratio of contact resistance to the total resistance.

5) Thinner materials experience faster temperature rise and lose more heat to the electrodes.

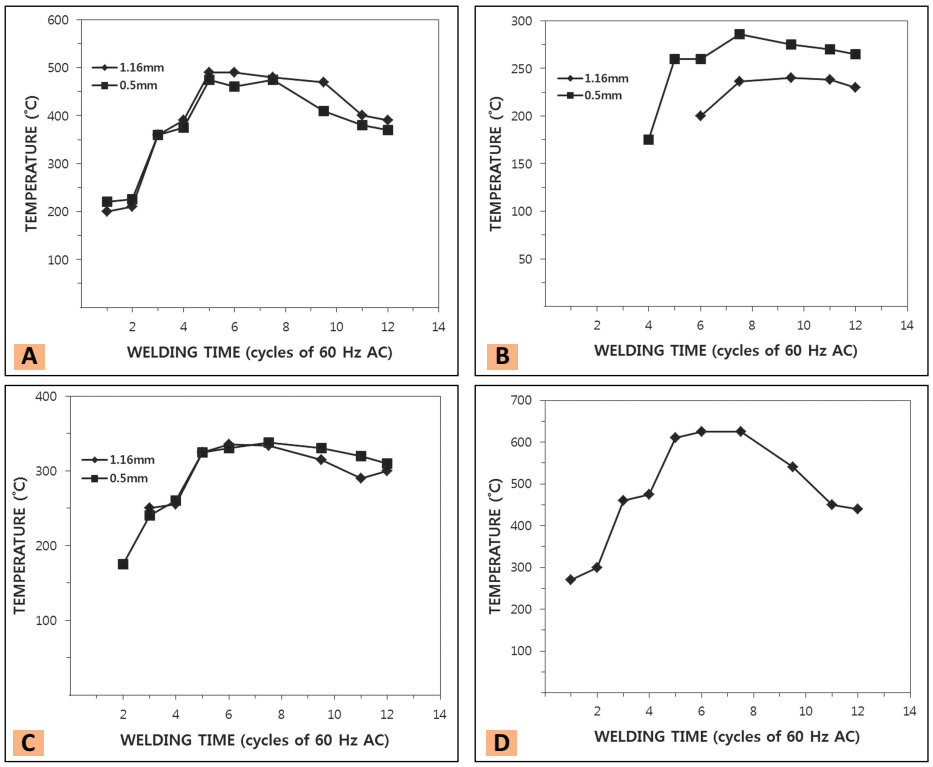

Fig. 12 — Temporal temperature changes at the electrode interface. A — At workpiece side; B — at 1.6 mm from the electrode interface; C — electrode interface at electrode side; D — at faying interface during simulated disk welding of bare steel of different thicknesses.

References

1. Kim, E. W., and Eagar, T. W. 1989. Measurement of transient temperature during resistance spot welding. *Welding Journal* 68(8): 303-s to 312-s.

2. Horita, T., Oka, M., Kanamaru, T., Yamazaki, K., and Fujiwara, T. 1996. Study of nugget formation in spot welding of galvanized steel sheet (selected from *Quarterly Journal of the Japan Welding Society* 14(2): pp. 255–259). *Welding International*: pp. 937–942.

3. Natale, T. V. 1986. A comparison of resistance spot weldability of hot dip and electrogalvanized sheet steel. SAE Technical Paper 860435.

4. Howe, P., and Kelly, S. C. 1988. A comparison of the resistance spot weldability of bare, hot-dipped, galvannealed, and electrogalvanized DQSK sheet steels. SAE paper 880280.

5. Aravinthan, A., and Nachimani, C. 2011. Analysis of spot weld growth on mild steel and stainless steel. *Welding Journal* 90 (8): 143-s to 147-s.

6. Chuko, W. L., and Gould, J. E. 2002. Development of appropriate resistance spot welding practice for transformation-hardened steels. *Welding Journal* 81(1): 1-s to 7-s.

7. Sun, X., Stephens, E. V., Khaleel, M. A., Shao, H., and Kimchi, M. 2004. Resistance spot welding of aluminum alloy to steel with transition materials — From process to performance — Part I: Experimental study. *Welding Journal* 83 (6): 188-s to 194-s.

8. Boron, S. 1998. An investigation into spot welding of zinc sheet. *Welding International* 12(12): 932–936.

9. Na, S. J., and Park, S. W. 1996. A theoretical study on electrical and thermal response in resistance spot welding. *Welding Journal* 75(8): 233-s to 241-s.

10. Sun, X. 2000. Modeling of projection welding process using coupled finite element analysis. *Welding Journal* 79(9): 244-s to 250-s.

11. Sun, X., and Khaleel, M. A. 2004. Resistance spot welding of aluminum alloy to steel with transition materials — Part II: Finite element analyses of nugget growth. *Welding Journal* 83(7): 197-s to 201-s.

12. Browne, D. J., Chandler, H. W., Evans, J. T., James, P. S., Wen, J., and Newton, J. 1995. Computer simulation of resistance spot welding in aluminum: Part II. *Welding Journal* 74(12): 417-s to 421-s.

13. Zhang, W. 2006. Recent advances and improvements in the simulation of resistance welding processes. *Welding in the World* 50(3/4): 29–37.

14. Zhang, Y. S., Xu, J., Lai, M., and Chen, G. L. 2008. Numerical simulation of spot welding for galvanized sheet steels. *Science and Technology of Welding and Joining* 13(2): 192–198.

15. Gedeon, S. A. 1984. Resistance spot welding of galvanized steel sheet. M.S. thesis, Massachusetts Institute of Technology.

16. McPherson, G. 1981. *An Introduction to Electrical Machines and Transformers*. John-Wiley & Sons.

17. Kim, E. 1989. Analyses of resistance spot welding lobe curve, ScD thesis, Massachusetts Institute of Technology.

18. Holm, R. 1967. *Electrical Contacts*, 4th ed., Springer-Verlag, New York.

19. Kim, E. 2002. Temperature dependent behavior of thermal and electrical contacts during resistance spot welding. *International Journal of Korean Welding Society* 2(1): 1–10.

20. Smithells. 1978. *Metal Reference Book*, 5th ed., Butterworths.

21. Song, Q., Zhang, W., and Bay, N. 2005. An experimental study determines the electrical contact resistance in resistance spot welding. *Welding Journal* 84(5): 73-s to 76-s.

22. Thornton, P. H., Krause, A.R., and Davies, R. G. 1996. Contact resistances in spot welding. *Welding Journal* 75(12): 402-s to 412-s.

23. Vogler, M., and Sheppard, S. 1993. Electrical contact resistance under high loads and elevated temperatures. *Welding Journal* 72(6): 231-s to 238-s.

24. Kim, E. W., and Eagar, T. W. 1988. Parametric analysis of resistance spot welding lobe curve. SAE Technical Papers 880278.

25. Yeung, K. S., and Thornton, P. H. 1999. Transient thermal analysis of spot welding electrodes. *Welding Journal* 78(1): 1-s to 6-s.